

Three-dimension Tip Force Perception and Axial Contact Location Identification for Flexible Endoscopy using Tissue-compliant Soft Distal Attachment Cap Sensors

Tao Zhang[†], Yang Yang^{†,1}, Yang Yang², Huxin Gao, Jiewen Lai and Hongliang Ren*

Abstract—In endoluminal surgeries, inserting a flexible endoscope is one of the fundamental procedures. During this process, vision remains the primary feedback, while the perception of tactile magnitude and location is insufficient. This limitation can hinder the clinician’s efficiency when navigating the endoscope through various segments of the natural lumens. To address this issue, we propose a fiber Bragg grating (FBG)-based tissue-compliant sensor cap with multi-mode sensing capabilities, including contact location identification at the terminal surface and the three-dimensional contact force perception at the tip. The soft sensor cap can be affixed to the standard endoscope tip, like a distal attachment cap, for easy installation. Utilizing the relative contact location information, operators can adjust the steerable segment of the endoscope when transitioning from one segment of a natural orifice to a narrower segment, which may be obstructed by constricted lumens. A finite element analysis simulation and the corresponding calibration process based on learning-based approaches have been carried out. The FBG-based sensor can perceive the tip contact force and identify the axial contact location with high precision, where the force perception error is less than 3%, and the contact location identification accuracy is 98.8%. The experimental results demonstrate the potential of the proposed sensing mechanism to be applied in surgeries requiring endoscope insertions.

I. INTRODUCTION

Endoscopic surgery refers to the minimally invasive surgical approach that performs surgeries through the natural orifices. This technique is characterized by no external incisions and minimal internal incisions, making it crucial for diagnosis and treatment in areas such as the oral cavity [1], nasal passages, and gastrointestinal tract [2]. However, in both manual and robot-assisted surgeries, tactile information at the distal tip of the endoscope is essential for accurately determining the contact situation and relative position between the endoscope tip and the luminal wall.

To sense the contact information between surgical tools and luminal tissue, various force-sensitive elements have

This work was supported in part by Hong Kong Research Grants Council (RGC) Collaborative Research Fund (CRF C4026-21GF), and General Research Fund (GRF 14216022), NSFC/RGC Joint Research Scheme N_CUHK420/22; Shenzhen-Hong Kong-Macau Technology Research Programme (Type C) Grant 202108233000303; Guangdong Basic and Applied Basic Research Foundation (GBABF) #2021B1515120035; CUHK Faculty Direct Grant (4055213).

T. Zhang, Y. Yang², H. Gao, J. Lai, and H. Ren are with the Department of Electronics Engineering, The Chinese University of Hong Kong, Hong Kong, China. {tzhang@link, y.yang@, huxinggao@, jwlai@ee, hlren@ee}.cuhk.edu.hk;

Y. Yang¹ is with the Department of Electronics Engineering, The Chinese University of Hong Kong, Hong Kong, China, and the Department of Mechanics Science and Engineering, Sichuan University, Chengdu 610065, China. youngyang@stu.scu.edu.cn.

[†]Tao Zhang and Yang Yang¹ have equal contribution.

*Corresponding author is Hongliang Ren.

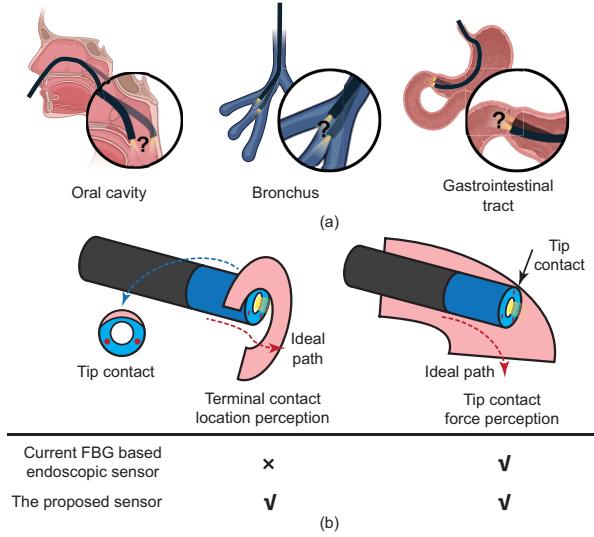


Fig. 1. Function illustration for the proposed sensor, MM-TCS, like a functionalized distal attachment cap. (a) Three typical intervention scenarios that require tip contact perception in endoscopy. (b) Tip contact type of the flexible endoscope when inserting a narrow lumen.

been attached to the surgical tools, such as piezoresistive materials [3], piezoelectric ceramic materials [4], optical fibers [5], [6], and elastic structures with pneumatic- [7], magnetic-driven mechanisms [8], or vision detectors [9]. Yue *et al.* [4] employed piezoelectric elements to carry out soft tissue palpation, and Rehan *et al.* [8] adopted magnetic elements to realize force feedback in robotic surgical systems. However, the dimension of the former sensors limits their application in endoscopic surgeries. Zhao *et al.* [7] proposed a pneumatic tactile sensor with a polydimethylsiloxane (PDMS) balloon as the sensitive element, which is linked to an extra pressure sensor via a long tube attached to the endoscope. Although the choice of PDMS makes it possible for the endoscope to acquire visual information passing through the balloon, the additional tube increases the endoscope dimension, which could negatively affect miniature endoscopes like bronchoscopes. Compared with the above sensors, the fiber Bragg grating (FBG) demonstrates a higher potential in perceiving operational information for minimally invasive surgical instruments, leveraging its advantage of compact dimension. Lai *et al.* [10] integrated three FBGs with a flexible grasper (the diameter is 4.2 mm) to sense three-dimension (3D) operation forces. Gao *et al.* [11] integrated optical fibers inscribed with multiple FBGs with a notch continuum manipulator to perceive the radial contact location along the manipulator, while the paper did not identify

the contact location at the terminal surface. Additionally, FBG-based force sensors for flexible catheters have been researched [12], and the miniature FBG fibers (0.25 mm, including the protective layer) can be easily integrated inside the catheter. Further, to enhance the safety of the flexible endoscope, Zhang *et al.* [13] replaced the rigid backbone with a flexible one made from PDMS. This sensor performs well in 3D force sensing. However, the rigid plate fixed at the distal tip still limits the sensing capability of the multiple fibers compared to a fully flexible sensor.

Several fully flexible sensors have been proposed in the robotics field, such as flexible grippers [14], [15], tissue palpation [16] and artificial vein [17] and skin [18]. These studies usually utilize a sensor array made of optical fibers [19], balloons [20], and other sensitive materials to obtain more contact details besides the contact force, such as the shape and location of the object in contact. However, these sensors mainly focus on the contact applied to their terminal surface, and the current array configurations can not fit the flexible endoscopes directly.

As shown in Fig. 1, when inserting an endoscope into the natural orifice, there are two types of contact: axial contact applied to the terminal surface and radial contact applied to the tip. To detect these contacts, the sensor is expected to perceive the radial force and the axial force and identify the contact location at the terminal surface.

To meet the requirements of the contact feedback in endoscopes, this work proposed an FBG-based multi-mode (radial force, axial force, and axial contact location) tissue-compliant sensor (MM-TCS) for flexible endoscopes.

The core contributions of this work include the following:

- FBG-based tissue-compliant tactile sensor with 3D force sensing and forehead axial contact location identification capability, which can be well-affixed to the endoscopic tip like distal attachment cap of standard flexible endoscopes for *in situ* multimodal perception.
- The learning-based tactile sensing approach has been proposed to overcome the modeling difficulties caused by the anisotropy of sensor stiffness.

II. WORKING PRINCIPLE OF THE PROPOSED SENSOR

A. Materials and design

Fig. 2 demonstrates a flexible endoscope equipped with the MM-TCS at the distal tip and the detailed structure of the MM-TCS. The outer diameter of the endoscope is 5.6 mm, the length of the steerable segment is 36 mm, and an endoscopic camera is attached to the working channel.

A fully flexible structure is adopted to design and fabricate the MM-TCS to obtain tip contact force information and the contact location at the terminal surface. The backbone of the MM-TCS is made of EcoFlex Dragon Skin 20. Considering that the flexible structure will lead to significant deformation compared with the sensor with a high-stiffness structure, the FBGs are directly embedded in the silicone to avoid accidents such as FBG breakage or uneven contact between the FBGs and the soft backbone. In the center of the backbone, there is a flexible working channel to accommodate the endoscopic camera. The sensitive elements

of the MM-TCS are three evenly distributed FBGs for contact perception and one extra FBG for temperature compensation. At the terminal surface of the MM-TCS, there is a protective layer made of EcoFlex Dragon Skin 20, which protects the terminal surface of the FBGs. In addition, if there is a need to add different surgical tools to the endoscope, an extra working channel can be easily added, as the diameter of the FBG is only 0.25 mm.

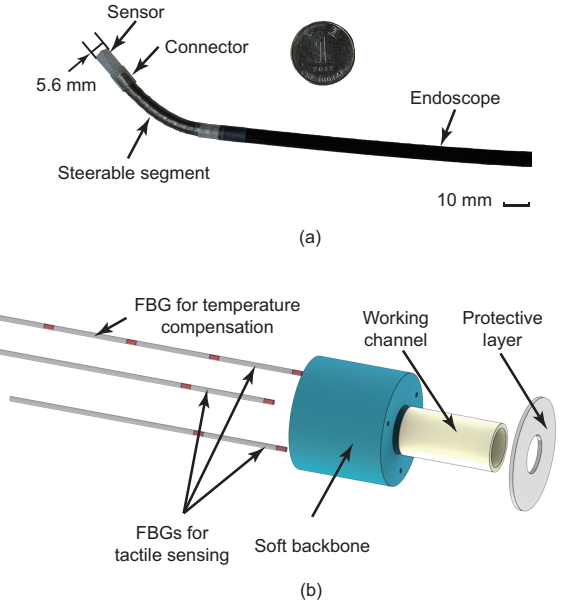


Fig. 2. The flexible endoscope equipped with the MM-TCS like a distal attachment cap. (a) The main structure of the flexible endoscope's steerable segment and sensing segment. (b) The detailed structure of the proposed MM-TCS.

B. Working principle

In the MM-TCS, the sensitive elements are FBGs, which follow the principle of wavelength-selective reflection. When a broadband light source is coupled into an FBG, the light with the particular wavelength (Bragg wavelength) will be reflected while others will pass through the FBG. The Bragg wavelength is sensitive to variations in both the strain experienced by the FBG and the ambient temperature, and the principle is shown in Eq. (1).

$$\frac{\Delta\lambda_i}{\lambda_i} = \varepsilon_i(1 - \rho_e) + \zeta\Delta T, \quad (1)$$

where $\Delta\lambda_i$ and λ_i are the wavelength shift and the initial wavelength of the i -th FBG, ε_i is the strain of the i -th FBG, ρ_e is the effective photo-elastic coefficient, ζ is the thermal-optic coefficient, and ΔT is the temperature change.

The principle of the strain change is illustrated in Fig. 3. For the MM-TCS, which can be treated as a flexible cylinder, when there is an eccentric axial contact at its terminal surface, the MM-TCS tends to experience non-uniform compression and bending due to eccentric axial contact. However, in the working scenario, the axial contact that needs to be identified is large enough to prevent the endoscope insertion, which means the eccentricity degree of the contact is low. In addition, the length-diameter ratio of the MM-TCS is $5/5.6 = 0.89$, which renders the MM-TCS

less susceptible to bending under axial forces. As a result, the bending can be inconspicuous enough to be ignored. Then, the deformation of the MM-TCS can be depicted as Fig. 3(b). The length shifts of the three FBGs follow Eq. (2).

$$k_1 \Delta l_1 = k_2 \Delta l_1 = k_3 \Delta l_1 = \frac{l_0 P_a F_a}{EA}, \quad (2)$$

where P_a is the contact location, F_a is the magnitude of the contact force, EA is the equivalent compression stiffness which is related to the axial contact location, k_i is a coefficient considering the strain transformation between the silicone and the i -th FBG, which is related to the contact location and the stiffness difference between the silicone and the FBG. $\Delta l_i = l_i \varepsilon_i = l_0 - l_i$ is the length shift of the i -th FBG (l_0 is the initial length of the MM-TCS).

Combining Eq. (1) and (2), the correlation between wavelength shifts and axial contact force can be formulated as Eq. (3).

$$\Delta \lambda_i = \lambda_i (1 - \rho_e) \frac{F_a}{k_i EA} + \lambda_i \zeta \Delta T. \quad (3)$$

When a radial force is applied to the sensor, the deformation of the sensor is bending in the direction of the external force, as shown in Fig. 3(c). According to the research on flexible robots [2], when the bending angle of a flexible rod is small, the post-deformed shape of the rod can be treated as an arc. As a result, when a radial force is applied, the MM-TCS can be modeled as an arc with the central angle θ . As illustrated in Fig. 3, d_i is the distance from the i -th FBG to the neutral plane, and the sign of it depends on whether the corresponding FBG is extended or shortened. Additionally, the distance between the FBG and the central axis of the MM-TCS is R , the bending radius is r , and φ denotes the orientation of the radial force. Then, the length of each FBG can be calculated as

$$\begin{cases} \Delta l_i = l_i \varepsilon_i = \eta ((r + d_i) \theta - r\theta) = \eta d_i \theta \\ d_i = -R \cos(\varphi + 120^\circ (i-1)), i = \{1, 2, 3\} \\ \theta = \frac{F_r l_0}{E_b(\varphi) A} \end{cases}, \quad (4)$$

where $E_b(\varphi) A$ is the equivalent bending stiffness of the MM-TCS, considering that the significant stiffness difference between FBG and silicone leads to deformation dissonance, the equivalent bending stiffness of the MM-TCS varies along the deflection angle φ . Additionally, F_r is the magnitude of the radial force, η is the correction coefficient considering the deformation dissonance.

Combining Eq. (1) and (4), the correlation between wavelength shifts and radial forces can be formulated as Eq. (5).

$$\Delta \lambda_i = \lambda_i (1 - \rho_e) \frac{\eta d_i l_0}{l_i E_b(\varphi) A} F_r + \lambda_i \zeta \Delta T. \quad (5)$$

Refer to Eq. (3) and Eq. (5), when the MM-TCS is subjected to axial or radial external forces, the wavelength shifts can consistently be represented as a function of both contact force and temperature.

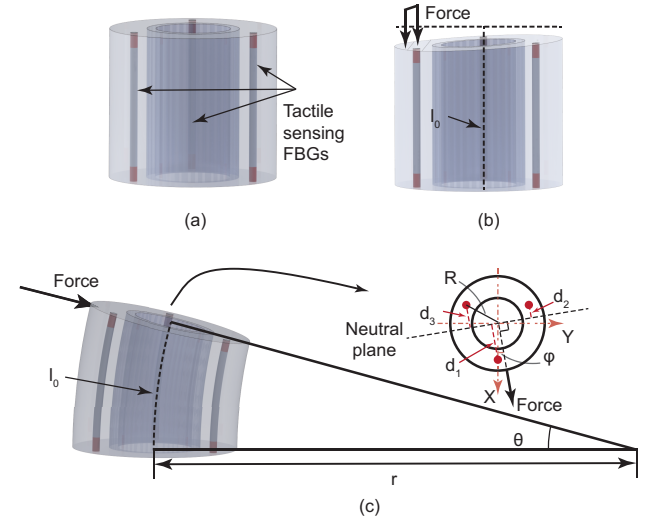


Fig. 3. Working principle: (a) Initial structure of the MM-TCS. (b) MM-TCS under axial force. (c) MM-TCS under radial force.

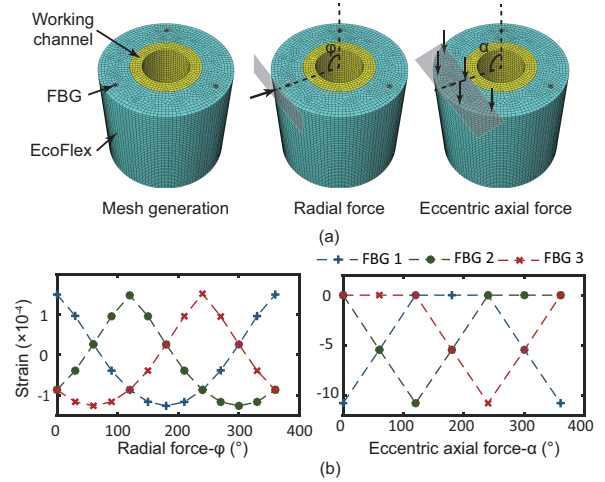


Fig. 4. FEA simulation of the MM-TCS. (a) The mesh generation of the MM-TCS. (b) The relationship between the FBGs' strain and the radial forces from different directions/the contact location of the axial forces.

C. Finite Element Analysis Simulation

ABAQUS/Standard-based finite element analysis (FEA) simulation was employed to assess the effectiveness of the sensing capability of the MM-TCS. The main content of the FEA is shown as follows:

1) *Material Parameters*: The soft backbone, optical fibers, and working channel material parameters are shown in Table I.

2) *Mesh*: The mesh generation results are shown in Fig. 4(a). The simplified integration hexahedral 8-node element (C3D8R) is adopted to generate the results.

3) *Interaction*: The interaction between each material is modeled as a binding constraint. The plant for applying loads is considered a rigid body.

4) *Loading and boundary condition*: The base of the sensor is secured, and two contact scenarios are simulated at its tip. The first involves radial forces, and the second involves axial forces applied to different regions (Fig. 4(a)). To facilitate the distinction, the direction of the radial contact

force is represented by φ , and the angle of the axial contact location identification is represented by α .

5) Results: The simulation results (Fig. 4(b)) indicate that when the direction of the radial force or the application location of the eccentric axial force changes, the wavelength shifts of the FBGs will correspondingly vary, leading to a corresponding change in the wavelength shift ratio among the different FBGs. Additionally, the asymmetric strain variation of the FBGs under radial forces from varying directions also illustrates the anisotropy of sensor stiffness, which corresponds to the $E_b(\varphi)A$ in Eq. (4).

TABLE I
MATERIAL PARAMETERS SETTINGS IN THE FEA SIMULATION

Part of sensor	Material	Young's modulus (MPa)
Soft backbone	EcoFlex Dragon Skin 20	0.3378
Optical fibers	Silica	72,000
Working Channel	Silicone Rubber	9.5

III. MANUFACTURING PROCESS

The manufacturing process of the MM-TCS is shown as follows. First, the tactile sensing FBGs are fixed in a specially designed mold, ensuring they are parallel to each other and in the desired positions. In addition, a pre-tension is applied to prevent the FBGs from becoming slack. Then, the silicone is poured into the mold to form the initial sensor. Once the silicone has solidified, the FBGs are secured to the silicone backbone using glue, and the excess fibers will be removed. Finally, to protect the terminal surface of the FBGs, an extra protective layer made of silicone is added. The soft property of this layer ensures the ability of the MM-TCS to perceive contact information at its terminal surface.

IV. SENSOR CALIBRATION

Calibration experiments have been carried out to verify the working performance of the MM-TCS. The calibration setup is depicted in Fig. 5. A platform with multiple degrees of freedom (DoF) has been adopted to adjust the orientation of the force. The ATI force sensor (Nano17, ATI Industrial Automation, NC, USA) is employed to measure the contact force. The wavelengths of the FBGs are obtained through an optical FBG interrogator (OPM-T1620, Gaussian Optics Company Ltd., China). Additionally, the ATI sensor holder configuration is adjusted to apply either radial or axial forces.

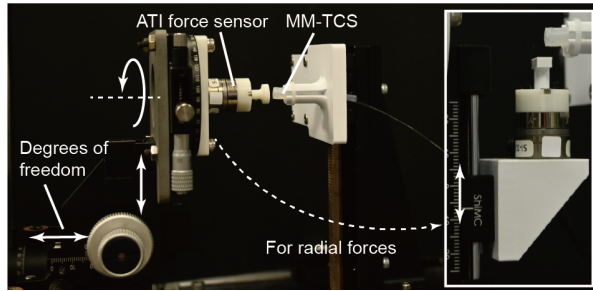


Fig. 5. The calibration setup of the MM-TCS. To apply the radial and axial forces, the ATI sensor holder needs to be changed to adjust the relative position.

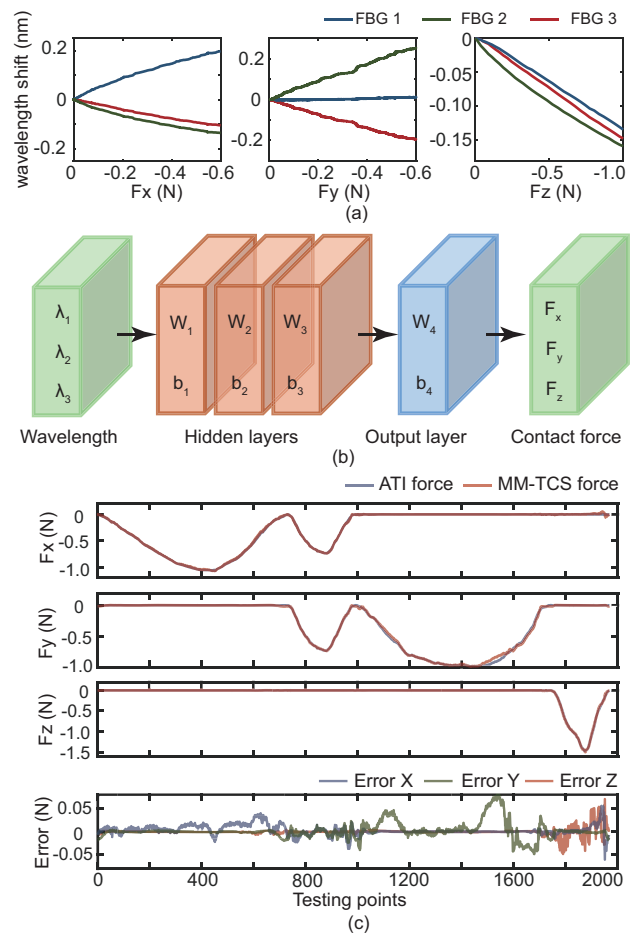


Fig. 6. Contact force calibration. (a) Relationship between the wavelength shift and the contact force. (b) The structure of the learning-based model. (c) The perception results and perception error of F_x , F_y and F_z .

A. Contact force calibration

The simulation results have shown that when the contact forces from different directions are applied to the MM-TCS, the wavelength shifts vary with the direction and magnitude of the external forces. In this experiment, a continuum load is applied to the MM-TCS, Fig. 6(a) illustrates the correlation between the wavelength shift and the contact force in X, Y, and Z direction. In this paper, the force is considered negative when it is directed toward the central axis or from the distal tip to the proximal tip.

Considering that the fabrication errors and anisotropy of sensor stiffness, the model-based calibration will lead to higher perception error and complexity. Therefore, we employ a learning-based approach to calibrate the proposed MM-TCS. The diagram of the Neural Network (NN) model is represented in Fig. 6(b). The input and the output of the NN are the wavelength shift of each FBG and the external force applied to the sensor. The NN model adopts three hidden layers and an output layer to model the soft sensor. In addition, each hidden layer has six neurons.

To validate the accuracy of the former learning-based approach, the radial forces from three different directions ($\varphi = 0^\circ$, 45° and 90°) and a concentric axial force has been

applied to the MM-TCS. The results (Fig. 6(c)) demonstrate that the proposed MM-TCS can accurately perceive forces from different directions. The mean square error of the prediction is 0.022 N, which is less than 3% over the maximum contact force.

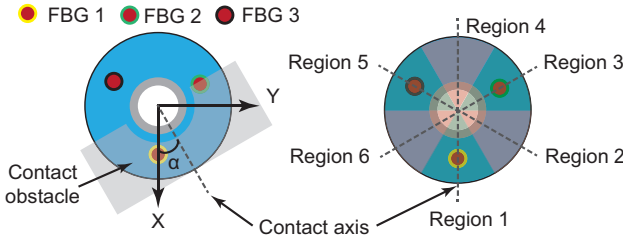


Fig. 7. Contact statement: To show the relationship between the contact location and the FBGs, the protective layer is hidden. The gray shadow refers to the contact obstacle, and the contact location is expressed by its symmetry axis, the contact axis. α refers to the deflection angle of the contact axis, and the terminal surface of the sensor is divided into six regions.

B. Contact location identification

In this working scenario, we apply several eccentric contacts from different contact locations. As shown in Fig. 7, the gray shadow denotes the contact obstacle applied to the MM-TCS, and the contact location is indicated by its central axis, which is denoted by the contact axis. Considering the real working environment, the contact region will not cover the working channel in each contact, or the endoscopic camera can easily perceive the contact location. The shape of the contact obstacle is designed as a semi-circular notch to simulate the irregularity of the contact surface. In addition, the terminal surface of the sensor is divided into six regions, each with a center angle of 60° . When different contacts are applied, the wavelength shifts of each FBG are shown in Fig. 8. In each sub-figure, the horizontal axis refers to the press process. The results indicate that when contact is applied from different locations, the wavelength shift ratios differ, demonstrating that the FBGs of the MM-TCS have the function of a sensor array on the terminal surface and can respond to axial contacts from different contact locations.

The decision tree model is adopted to identify the contact location when an eccentric axial contact is applied to the MM-TCS. The input of this model is the normalized wavelength shifts of the three tactile sensing FBGs. The output of the model is the contact location type, which is labeled as region_{*i*}. In this paper, the location type refers to the region the contact axis belongs to. To ensure the universality of the contact location identification method, the specific contact axis of each contact type is evenly selected within the corresponding contact location.

The identification result is shown in Fig. 8(c). In this figure, the vertical axis represents the actual contact location, and the horizontal axis represents the contact location predicted by the decision tree model. The results demonstrate that the proposed MM-TCS can sense the contact location accurately. When the contact location is divided into six types and the number of the tests is 600 (100 times for each location type), the predicted accuracy of each contact location is higher than 96%, with an overall accuracy rate of

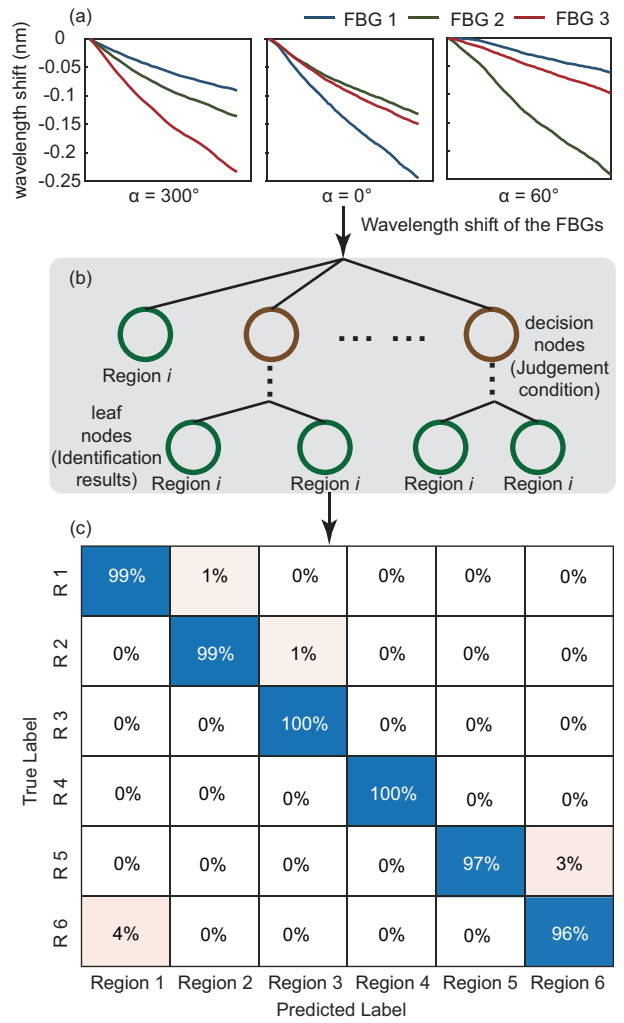


Fig. 8. Contact location identification: (a) Relationship between the wavelength shift and the contact regions. The deflection angle of the contact axis is $300^\circ/0^\circ/60^\circ$. (b) The decision tree model structure. (c) The experimental results of the contact region identification.

98.8%. The main error occurs between the adjacent location types due to the similar contact conditions between them.

V. TEMPERATURE COMPENSATION

The above work is conducted at room temperature. However, the human body temperature is higher than the room temperature, varying from 36°C to 40°C . To compensate for temperature variations, an extra FBG is added to one of the fibers (Fig. 2). The wavelength shift caused by temperature variation does not impact the wavelength shift caused by the strain. Therefore, we can directly compensate for temperature variations by adding the extra temperature-sensing FBG.

In this work, the temperature of the MM-TCS is adjusted using a thermostat, with a control range from 36° to 42° . The wavelength shifts of the FBGs are shown in Fig. 9. Specifically, FBG 4 refers to the FBG used to sense the temperature, while FBG 1, 2, and 3 are used for tactile sensing. In this work, we set the room temperature as the initial state, and the wavelength shifts caused by the temperature variations can be expressed by a linear function, which can be shown as Eq. (6).

$$\begin{bmatrix} Ws_1 \\ Ws_2 \\ Ws_3 \\ Ws_4 \end{bmatrix} = \begin{bmatrix} 0.0133 \\ 0.0141 \\ 0.0141 \\ 0.0130 \end{bmatrix} T + \begin{bmatrix} -0.3534 \\ -0.3802 \\ -0.3810 \\ -0.3560 \end{bmatrix}, \quad (6)$$

where Ws_i is the wavelength shift of the i -th FBG, T is the environmental temperature.

According to the above function, the environmental temperature can be obtained by FBG 4, and the wavelength shifts of FBG 1, 2, and 3 can be compensated. The compensation results are shown in Fig. (6), and the dashed lines represent the wavelength shifts after temperature compensation, demonstrating that the proposed methods can effectively compensate for wavelength shifts caused by the temperature variation.

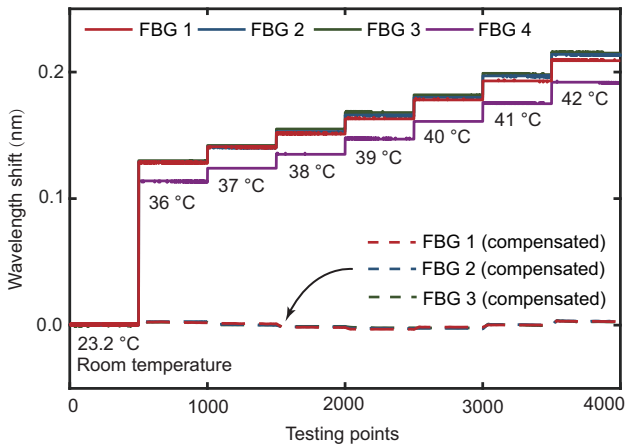


Fig. 9. Wavelength shifts of the FBGs under a varying temperature. The solid line represents the wavelength shift of each FBG, and the dashed line represents the wavelength shift after temperature compensation

VI. EXPERIMENTS

In this section, to further verify the working performance of the MM-TCS, phantom experiments to insert the endoscope via the natural orifices have been conducted.

Two phantom experiments have been carried out to validate the contact force perception function of the MM-TCS (Fig. 10). At first, the flexible endoscope with the MM-TCS is inserted into two orifices through the nasal cavity with different curvatures to show the perception capability. The curvature of the endoscope during the first insertion is lower than during the second insertion. The results show that when the endoscope is inserted into the natural orifice with higher curvature, the predicted contact force is also more potent than that for the insertion with lower curvature; the resultant force of insertion 1 is 0.1 N while insertion 2 is over 0.2 N. These results mean that the proposed MM-TCS can sense and warn of the large contact forces. Additionally, the direction of the contact force can be judged by analyzing the component force in each direction. The contact force direction for insertion 1 is along the X direction, and the contact force direction for insertion 2 is between the X and Y directions (φ varies from 0.82 rad to 0.72 rad).

Then, the endoscope is utilized to insert the target bronchus. As shown in Fig. 10(b), the initial view illustrates

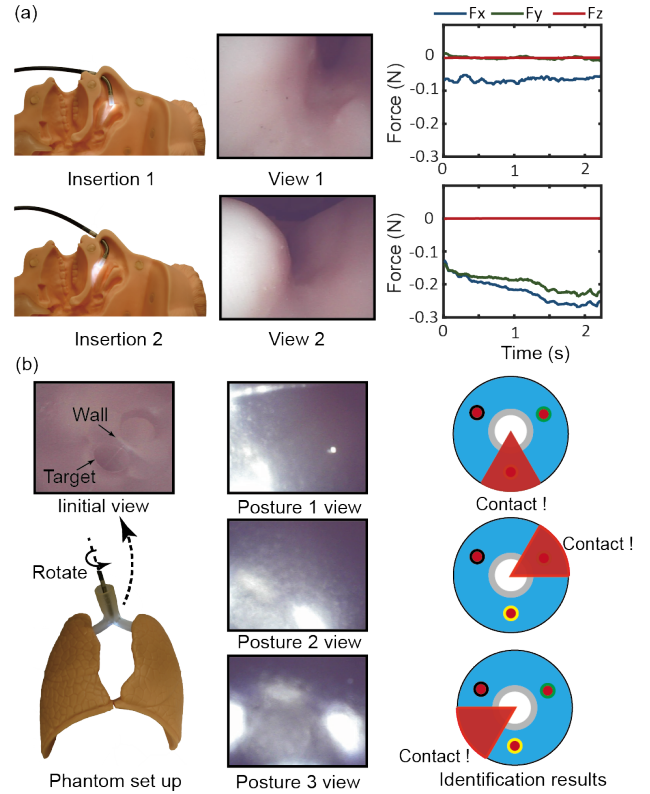


Fig. 10. The phantom experiments for the proposed MM-TCS: (a) Nasotracheal intubation experiments to show the force sensing function of the MM-TCS. (b) Tracheal intubation experiments to show the contact location identification function.

the position of the two bronchi and the wall between them. To represent the contact location identification function, we insert the endoscope into the target bronchus with different postures and make the terminal surface contact with the wall. Then, the position of the wall relative to the endoscope can be represented by the contact location at the terminal surface. During three attempts, we rotate the endoscope in the same direction, and the proposed decision tree model can identify the contact location, while we can not determine the wall through the vision feedback in these scenarios.

VII. CONCLUSIONS

In this paper, an FBG-based tissue-compliant sensor, MM-TCS, has been proposed to sense the contact force and the terminal surface contact location when inserting a flexible endoscope. Three parallel FBGs are employed to sense the multi-modal tactile information, and an extra FBG is added to compensate for the temperature impact. The calibration and phantom experiments verified the working performance of the proposed sensor, and the MM-TCS can be well-affixed to the endoscopic tip like a standard distal attachment cap. By integrating such a sensor into an endoscope, the clinician can obtain more information that can not be received by the endoscopic camera and finish the insertion task with increased security and efficiency.

REFERENCES

- [1] J. Lai, T.-A. Ren, W. Yue, S. Su, J. Y. Chan, and H. Ren, "Sim-to-real transfer of soft robotic navigation strategies that learns from the virtual

- eye-in-hand vision," *IEEE Transactions on Industrial Informatics*, 2023.
- [2] H. Gao, X. Yang, X. Xiao, X. Zhu, T. Zhang, C. Hou, H. Liu, M. Q.-H. Meng, L. Sun, X. Zuo *et al.*, "Transendoscopic flexible parallel continuum robotic mechanism for bimanual endoscopic submucosal dissection," *The International Journal of Robotics Research*, vol. 43, no. 3, pp. 281–304, 2024.
 - [3] C. Hou, K. Wang, F. Wang, H. Li, L. Lou, S. Zhang, Y. Gu, H. Liu, T. Chen, and L. Sun, "A highly integrated 3d mems force sensing module with variable sensitivity for robotic-assisted minimally invasive surgery," *Advanced Functional Materials*, vol. 33, no. 43, p. 2302812, 2023.
 - [4] W. Yue, F. Bai, J. Liu, F. Ju, M. Q.-H. Meng, C. M. Lim, and H. Ren, "Rasec: Rescaling acquisition strategy with energy constraints under fusion kernel for active incision recommendation in tracheotomy," *IEEE Transactions on Automation Science and Engineering*, 2024.
 - [5] T. Li, J. Guo, H. Zheng, S. Wang, L. Qiu, and H. Ren, "Fault-tolerant six-axis fbg force/moment sensing for robotic interventions," *IEEE/ASME Transactions on Mechatronics*, vol. 28, no. 6, pp. 3537–3550, 2023.
 - [6] Y. Tang, H. Liu, J. Pan, Z. Zhang, Y. Xu, N. Yao, L. Zhang, and L. Tong, "Optical micro/nanofiber-enabled compact tactile sensor for hardness discrimination," *ACS applied materials & interfaces*, vol. 13, no. 3, pp. 4560–4566, 2021.
 - [7] S. Zhao, C. C. Nguyen, T. T. Hoang, T. N. Do, and H.-P. Phan, "Transparent pneumatic tactile sensors for soft biomedical robotics," *Sensors*, vol. 23, no. 12, p. 5671, 2023.
 - [8] M. Rehan, M. M. Saleem, M. I. Tiwana, R. I. Shakoor, and R. Cheung, "A soft multi-axis high force range magnetic tactile sensor for force feedback in robotic surgical systems," *Sensors*, vol. 22, no. 9, p. 3500, 2022.
 - [9] A. Padmanabha, F. Ebert, S. Tian, R. Calandra, C. Finn, and S. Levine, "Omnitact: A multi-directional high-resolution touch sensor," in *2020 IEEE International Conference on Robotics and Automation (ICRA)*. IEEE, 2020, pp. 618–624.
 - [10] W. Lai, L. Cao, J. Liu, S. C. Tjin, and S. J. Phee, "A three-axial force sensor based on fiber bragg gratings for surgical robots," *IEEE/ASME Transactions On Mechatronics*, vol. 27, no. 2, pp. 777–789, 2021.
 - [11] A. Gao, Z. Lin, C. Zhou, X. Ai, B. Huang, W. Chen, and G.-Z. Yang, "Body contact estimation of continuum robots with tension-profile sensing of actuation fibers," *IEEE Transactions on Robotics*, 2024.
 - [12] T. Li, C. Shi, and H. Ren, "Three-dimensional catheter distal force sensing for cardiac ablation based on fiber bragg grating," *IEEE/ASME transactions on mechatronics*, vol. 23, no. 5, pp. 2316–2327, 2018.
 - [13] Y. Zhang, Q. Jiang, F. Wang, J. Wang, M. Ye, and D. Li, "Tactoscope: An endoscope integrated with soft sensor for real-time tactile feedback," *Measurement*, vol. 235, p. 114953, 2024.
 - [14] Q. Liang, W. Xiao, J. Long, and D. Zhang, "A multimodal robust recognition method for grasping objects with robot flexible grippers," *IEEE/ASME Transactions on Mechatronics*, 2024.
 - [15] S. Frishman, J. Di, Z. Karachiwalla, R. J. Black, K. Moslehi, T. Smith, B. Coltin, B. Moslehi, and M. R. Cutkosky, "A multi-axis fbg-based tactile sensor for gripping in space," in *2021 IEEE/RSJ International Conference on Intelligent Robots and Systems (IROS)*. IEEE, 2021, pp. 1794–1799.
 - [16] M. Pulcinelli, L. Zoboli, F. De Tommasi, C. Massaroni, V. Altomare, A. Grasso, A. Gizzi, E. Schena, and D. L. Presti, "A multi-sensor tactile system based on fiber bragg grating sensors for soft tissue palpation," *IEEE Sensors Journal*, 2024.
 - [17] Q. Zhao, J. Lai, and H. K. Chu, "Reconstructing external force on the circumferential body of continuum robot with embedded proprioceptive sensors," *IEEE Transactions on Industrial Electronics*, vol. 69, no. 12, pp. 13111–13120, 2021.
 - [18] T. Li, Y. Su, H. Zheng, F. Chen, X. Li, Y. Tan, and Z. Zhou, "An artificial intelligence-motivated skin-like optical fiber tactile sensor," *Advanced Intelligent Systems*, vol. 5, no. 8, p. 2200460, 2023.
 - [19] B. Mao, K. Zhou, Y. Xiang, Y. Zhang, Q. Yuan, H. Hao, Y. Chen, H. Liu, X. Wang, X. Wang *et al.*, "A bioinspired robotic finger for multimodal tactile sensing powered by fiber optic sensors," *Advanced Intelligent Systems*, p. 2400175, 2024.
 - [20] N. Tano and T. Hatsuzawa, "Balloon-integrated pneumatic tactile sensor for tissue palpation in minimally invasive surgery," *Sensors and Actuators A: Physical*, vol. 363, p. 114772, 2023.